

Unusual strong ferromagnetism in site-ordered cubic Laves phase compound LuInCo_4 with Co-pyrochlore lattice

Taiki Shiotani,* Takeshi Waki, Yoshikazu Tabata, and Hiroyuki Nakamura
Department of Materials Science and Engineering, Kyoto University, Kyoto 606-8501, Japan

Hiroto Ohta
*Department of Molecular Chemistry and Biochemistry,
 Doshisha University, Kyotanabe 610-0321, Japan*
 (Dated: August 23, 2024)

We have successfully synthesized single crystals of the site-ordered cubic (C15b) Laves phase compound LuInCo_4 with the Co-pyrochlore sublattice for the first time. LuInCo_4 undergoes a ferromagnetic transition at 306 K and has a saturation moment of $3.43 \mu_B/\text{f.u.}$ at 5 K. The strongly ferromagnetic nature was verified by DFT calculations, suggesting that Co- $3d$ flat bands near the Fermi level induce the spin polarization. The magnetization is isotropic above ~ 100 K, saturates most easily in the [100] direction at low temperatures. In this anisotropic ferromagnetic state, the magnetization undergoes a metamagnetic transition in the [111] direction. Our results suggest that LuInCo_4 is a new strong but unusual itinerant electron ferromagnet, which deserves further study as a pyrochlore metal.

I. INTRODUCTION

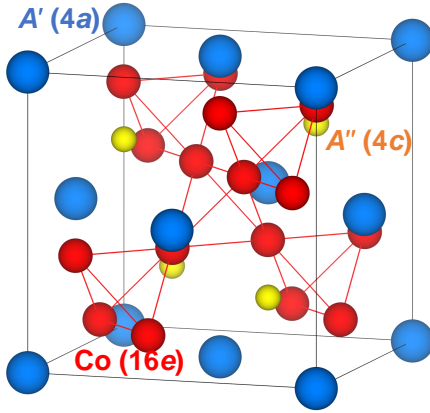


FIG. 1: Crystal structure of the C15b-type Laves phase compound. The A' site is occupied by a rare earth element, and A'' by Mg or In.

The interplay between unique lattice geometry and electronic correlations can lead to intriguing physical properties. The pyrochlore lattice, a network of corner-sharing tetrahedra, is a prototype of geometrically frustrated systems. Novel magnetic states due to frustration on the pyrochlore lattice have been discovered in a variety of insulators. Representative phenomena of the pyrochlore lattice are a spin ice in the rare-earth titanium oxides $\text{Dy}_2\text{Ti}_2\text{O}_7$ and $\text{Ho}_2\text{Ti}_2\text{O}_7$ [1, 2], spin glass in stoichiometrically pure $\text{Y}_2\text{Mo}_2\text{O}_7$ [3], and collective paramagnetism or spin liquid behavior in $\text{Tb}_2\text{Ti}_2\text{O}_7$ [4]. Although less explored than for insulators, the role

of the pyrochlore lattice on physical properties in the itinerant electron system is also being understood. For example, the C15 cubic Laves phase YMn_2 exhibits helical magnetic ordering with an extremely long period [5] and a spin-liquid state with small Sc substitution due to frustration on the Mn pyrochlore lattice [6]. Recently, non-trivial band structures in pyrochlore metals have also attracted attention. Analogous to the kagome lattice, a two-dimensional network of corner-sharing triangles, pyrochlore metals have been proposed to host three-dimensional flat bands due to quantum destructive interference [7, 8], which have been experimentally discovered in the C15 cubic Laves phase compound CaNi_2 and the thiospinel compound CuV_2S_4 [9, 10]. In addition, theoretical studies have predicted a four-fold degenerate Dirac point at the high symmetry point of the Brillouin zone [11–13].

A family of intermetallics with a Co pyrochlore lattice is known as the C15 Laves phase RCo_2 (R : rare-earth element). In RCo_2 , despite the large density of states (DOS) of the Co- $3d$ bands just below the Fermi level, the Co sublattice has no spontaneous magnetic moment, but the Co- $3d$ bands are magnetically polarized by the molecular field from the magnetic R sublattice [14]. Therefore, YCo_2 and LuCo_2 are exchange-enhanced Pauli paramagnets with high magnetic susceptibility and electronic specific heat coefficients [15–18]. Recently, a new series of cubic Laves phase RMgCo_4 ($R = \text{Y, Ce, Gd-Tm and Lu}$) with an A -site ordered (C15b) structure [Fig. 1] has been reported on synthesis and magnetism [19–24]. In RMgCo_4 , Co atoms occupy the Wyckoff position $16e$ (x, x, x), R atoms $4a$ ($0, 0, 0$), and Mg atoms $4c$ ($\frac{1}{4}, \frac{1}{4}, \frac{1}{4}$). Interestingly, RMgCo_4 has two frustrated sublattices: a breathing but nearly ideal pyrochlore sublattice formed by Co atoms and a face-centered cubic sublattice formed by R atoms, possibly leading to versatile quantum phases by changing the R atom. So far, YMgCo_4 has been

* Corresponding author: shiotani.taiki.48e@st.kyoto-u.ac.jp

reported to show strong ferromagnetism with a Curie temperature $T_C = 405$ K [21], in contrast to YCo_2 , while TbMgCo_4 has a ferrimagnetic structure where the Co moments are antiparallel to the Tb moments [23]. It is noteworthy that ^{59}Co -NMR measurements revealed that YMgCo_4 has widely distributed internal field at low temperature. This indicates that YMgCo_4 may not have a simple collinear structure, but rather a helically modulated ferromagnetic structure [21]. Although these features provide a new platform for exploring nontrivial magnetic phenomena in pyrochlore metals, it is limited to investigate the detailed physical properties. This is because the high vapor pressure of Mg makes it difficult to grow single crystals of RMgCo_4 .

In this context, we focused on RInCo_4 ($R = \text{Dy-Lu}$), which is isostructural with RMgCo_4 . Its presence and crystal structure have been reported by Sysa *et al.* in 1988 [25]. Because the $4c$ site is occupied by In instead of Mg, it is expected to be easier to synthesize single crystals. However, to date, there have been no reports on the growth and physical properties of the single crystals. In this paper, we report the single crystal synthesis of LuInCo_4 and discuss its magnetic properties based on magnetization measurements and density functional theory (DFT) calculations. We newly found that LuInCo_4 exhibits a ferromagnetic transition at $T_C = 306$ K with a saturation moment of $3.43 \mu_B/\text{f.u.}$ at $T = 5$ K. We also report a metamagnetic transition at low temperature under the field applied in the $[111]$ direction, suggesting that LuInCo_4 does not belong to the typical ferromagnets.

II. EXPERIMENTS

We have synthesized LuInCo_4 single crystals by the self-flux method starting from Lu ingots (Nippon Yttrium, 99.9% purity), In shots (Rare Metallic, 99.99%), and Co flakes (Rare Metallic, 99.9%). The mixture with a composition of LuIn_2Co_2 was arc-melted in an argon atmosphere, followed by grinding. The resulting mixture was placed in a BN crucible and sealed in an evacuated quartz tube. The ampoule was initially heated up to 1200°C over 3 h and held for 0.5 h, then cooled down to 1150°C over 8 h, and slowly cooled down to 975°C over 58h, at which the ampoule was centrifuged to separate single crystals from the flux. Octahedral or triangular crystals with well-developed $\{111\}$ faces were obtained. The flux and impurity phases remaining on the surface were removed by immersion in dilute HCl aq.

The grown crystals were characterized by x-ray diffraction (XRD) measurements with $\text{Cu } K_{\alpha 1}$ radiation using X'Pert PRO Alpha-1 (PANalytical). The Rietveld refinement was performed using Rietan-FP [26]. For this purpose powder was prepared by crushing a single crystal. Magnetization measurements were performed using a SQUID magnetometer (MPMS, Quantum Design) in

the temperature range of 5–350 K and under magnetic fields up to 7 T. We used octahedral crystals.

DFT calculations were performed using the Vienna *ab initio* simulation package (VASP) [27–30]. We used the projector augmented wave (PAW) pseudopotentials [31, 32] with the generalized gradient approximation (GGA) scheme following the Perdew, Burke and Ernzerhof (PBE) functional [33]. The conjugate gradient algorithm [34] was used for structural relaxation. The tetrahedron method with Blöchl corrections [35] and the Methfessel-Paxton scheme [36] were used for both geometry relaxation and total energy calculations. All atoms were relaxed until the forces on the atoms were less than 10^{-2} eV/Å and the energy difference between two successive electronic steps was less than 10^{-7} eV. The k -point mesh along the high symmetry path was set to 50.

III. RESULTS

A. Crystal structure

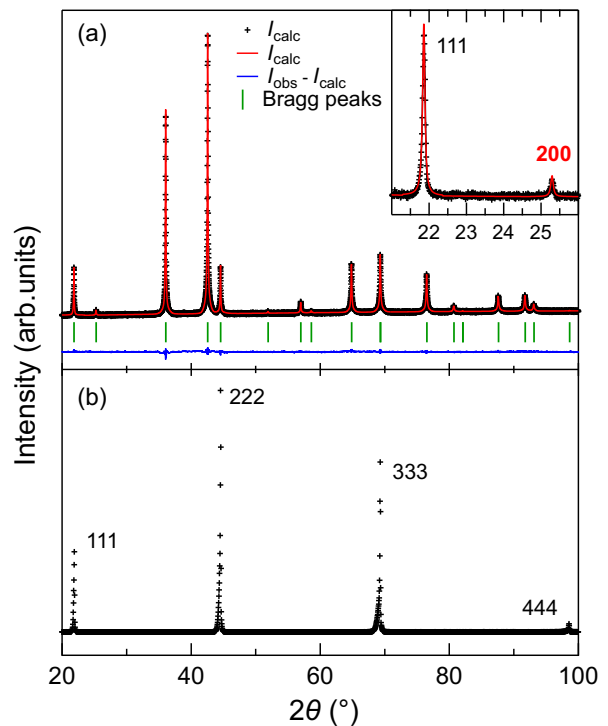


FIG. 2: (a) Powder XRD profile of LuInCo_4 at room temperature. The result of the Rietveld refinement and expected Bragg reflections are also shown. The inset shows the data in the extended 2θ range where the 200 superstructure peak is observed. (b) Monochromatic XRD pattern of the 111-surface of the LuInCo_4 single crystal.

Figure 2(a) shows the powder XRD profiles of LuInCo_4 at room temperature. We successfully obtained a single phase of LuInCo_4 . The 200 superstructure peak characteristic of the C15b-type structure was observed at $2\theta \simeq 25^\circ$ (see the inset of Fig. 2(a)), indicating that the reflection can be indexed by the planes of the site-ordered cubic Laves phase with space group $F\bar{4}3m$. The monochromatic XRD pattern collected from the flat surface of the single crystal showed the as-grown facet with the $\langle 111 \rangle$ direction perpendicular to the plate [Fig. 2(b)]. We performed structure refinement by the Rietveld method using Rietan-FP. Since optimizing all parameters at once resulted in negative isotropic displacement parameters B_{iso} , which are physically unreasonable, all B_{iso} were fixed as follows: $B_{\text{iso}}(\text{Lu}) = B_{\text{iso}}(\text{In}) = 0.75$ and $B_{\text{iso}}(\text{Co}) = 0.7$, with reference to literature data [24, 37]. The lattice parameter was estimated to be $a = 7.03874(1)$ Å, in agreement with literature data (7.029 Å [25]). The atomic coordinate at the Co 16e (x, x, x) site was calculated to be $x = 0.6252(2)$, which is close to that in the non-breathing pyrochlore lattice ($x = 0.625$). The nearest and next nearest neighbor intraatomic distances in the breathing pyrochlore lattice, 2.485(2) and 2.492(2) Å, respectively, are shorter than 2.53675 Å in the non-breathing pyrochlore lattice of LuCo_2 [38]. The site occupancy of Lu/In at the 4a site and In/Lu at the 4c site were 0.99(6)/0.01(7) and 0.87(6)/0.08(4), respectively, verifying the almost perfect atomic ordering of Lu and In in LuInCo_4 .

B. Magnetization

Figure 3 shows the temperature dependence of the magnetization of LuInCo_4 in the external field of $H_{\text{ext}} = 100$ Oe. It shows a ferromagnetic transition at a Curie temperature of $T_C \simeq 310$ K. The susceptibility above T_C was well fitted by the Curie-Weiss law $\chi = C/(T - \theta_W)$, where C is the Curie constant and θ_W is the Weiss temperature. The inverse susceptibility $1/\chi$ under the field applied in the [111] direction and its fitting result are shown in the inset of Fig. 3. The estimated value of $\theta_W = 313.8$ K is close to T_C , and suggests dominant ferromagnetic correlations in LuInCo_4 . The effective moment p_{eff} , estimated using the relation $C = \mu_B p_{\text{eff}}^2 / 3k_B$, is $3.22 \mu_B/\text{Co}$. These values do not depend significantly on the applied field direction. The magnetization begins to decrease below $T \simeq 150$ K, accompanied by a small bifurcation between zero-field-cooled and field-cooled data at $H_{\text{ext}} = 100$ Oe [Fig. 3]. The bifurcation becomes weaker with increasing field and almost disappears at $H_{\text{ext}} \simeq 1$ kOe. Figure 4 shows the temperature-dependent magnetization at different fields and its field derivatives. We found a peak in dM/dT at the low temperature. The corresponding temperature T^* and the temperature range where the

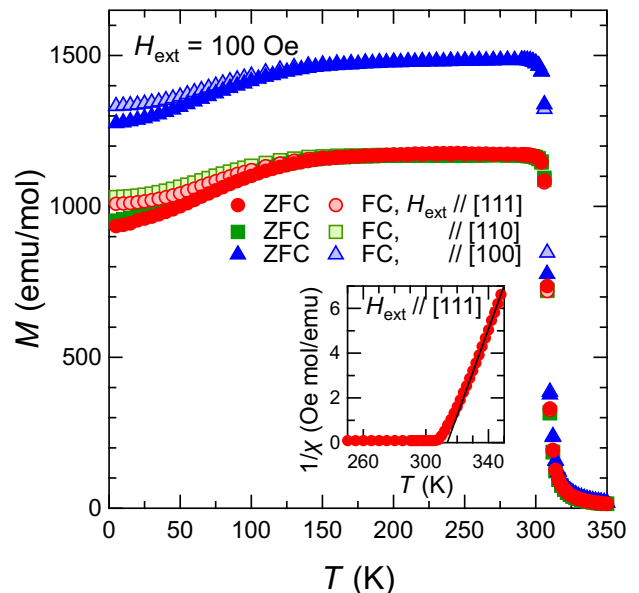


FIG. 3: Temperature dependence of the magnetization of LuInCo_4 at $H_{\text{ext}} = 100$ Oe. Open and filled markers represent the data under field-cooled and zero-field-cooled conditions, respectively. The inset shows the inverse susceptibility. The line represents the fit to the Curie-Weiss law.

magnetization is reduced change with the applied field strength. At $H_{\text{ext}} \simeq 1$ kOe in the [111] direction, T^* decreases. At $H_{\text{ext}} \simeq 5$ kOe, it reaches 0 K, resulting in a monotonic increase of the magnetization. We observed the same behavior for the field applied in the [110] direction. When $H_{\text{ext}} \parallel [100]$, the anomaly disappears at a lower field of $H_{\text{ext}} \simeq 2.5$ kOe [Fig. 4(b)].

1. Anisotropic magnetic isotherms

To reveal the magnetic anisotropy in LuInCo_4 , we measured the field-dependent magnetization at different temperatures. The crystal in the form of a regular octahedron was used, and the magnetic field was corrected by subtracting the demagnetizing field as $H = H_{\text{ext}} - NM$, where N is the demagnetization factor. N for the [100], [110], and [111] directions were calculated to be $N \simeq 0.31, 0.29$, and 0.29 , respectively, from the inverse slope of the low-field magnetization curve ($M(H_{\text{ext}})/H_{\text{ext}} \approx 1/D$) in the ferromagnetic state just below T_C . These nearly isotropic values close to $N = 1/3$ reflect that the regular octahedron has a geometry close to a sphere, leading to the validity of the estimate. Figure 5(a) shows the field dependence of the magnetization of the single crystal at $T = 5$ K. It shows ferromagnetic behavior with a saturation magnetization of $M_{\text{sat}} \simeq 3.43 \mu_B/\text{f.u.}$ The inset of Fig. 5(a) shows that the easy magnetiza-

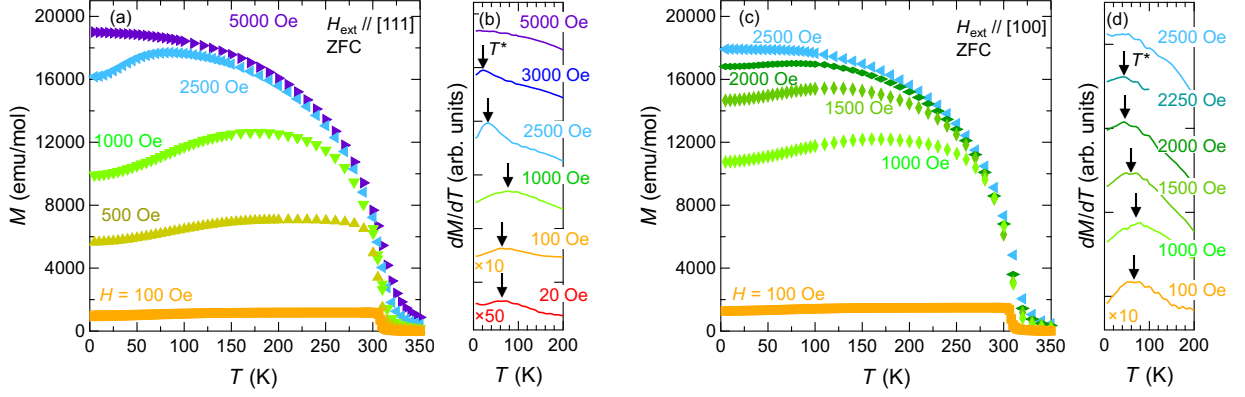


FIG. 4: (a)(c) Temperature dependence of the magnetization and (b)(d) its derivative dM/dT under magnetic fields along the [111] and [100] axes.

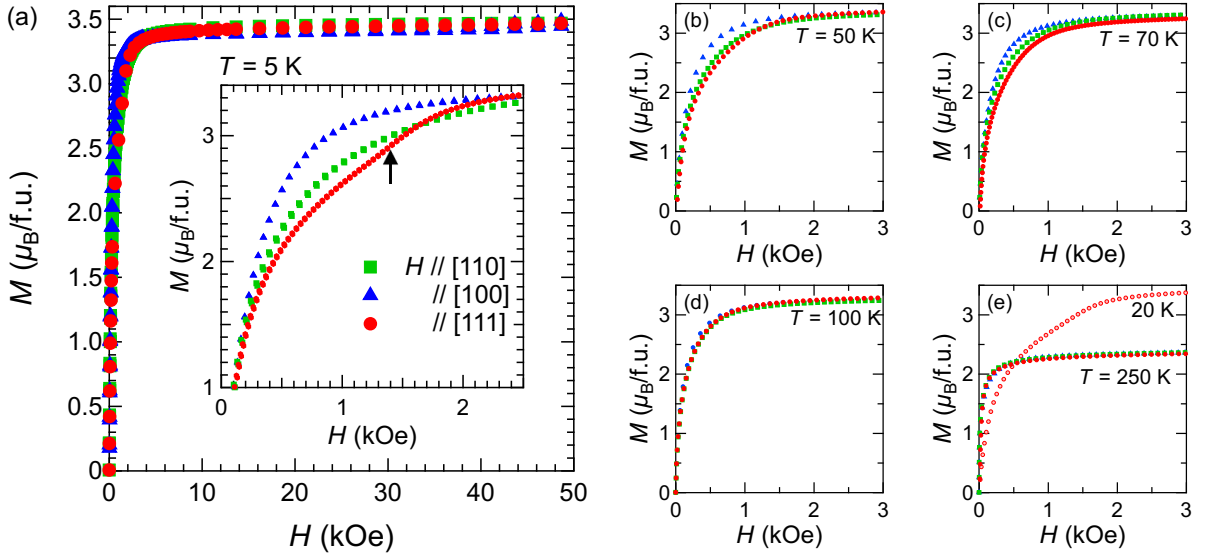


FIG. 5: Magnetization curves of LuInCo_4 at (a) $T = 5$ K, (b) 50 K, (c) 70 K, (d) 100 K, and (e) 250 K for the single crystal. The inset of Fig. 5(a) shows the data in the low-field region. The case of $T = 20$ K and $H \parallel [111]$ is also included in Fig. 5(e).

tion axis is in the [100] direction. As can be seen from Fig. 5, the difference in the magnetization between each crystallographic axis gradually becomes less pronounced with increasing temperature, and the magnetization process becomes isotropic above $T = 100$ K. The slope of the magnetization in the low field is larger at the higher temperatures (see Fig. 5(e)). This means that the magnetization saturates more easily in the high temperature region, which is in accordance with the small reduction in the temperature-dependent magnetization at low temperature.

The anisotropy energy of a cubic ferromagnet can be written simply as

$$E_A = K_0 + K_1(a_1^2 a_2^2 + a_2^2 a_3^2 + a_3^2 a_1^2) + K_2 a_1^2 a_2^2 a_3^2, \quad (1)$$

where K_0 , K_1 and K_2 are the anisotropy constants and a_1 , a_2 , a_3 are the directional cosines of the magnetization with respect to the cubic axes. K_1 and K_2 can be estimated thermodynamically. The energy required to magnetize a crystal to saturation ($M = M_{\text{sat}}$) in a direction $[hkl]$ is given by $E_{hkl} = \int_0^{M_{\text{sat}}} H_{hkl} dM_{hkl}$. Comparing E_A and E_{hkl} , K_1 and K_2 can be expressed as follows:

$$K_1 = 4(E_{110} - E_{100}), \quad (2)$$

$$K_2 = 9(E_{100} + 3E_{111} - 4E_{110}). \quad (3)$$

Evaluating the area of the magnetization process up to saturation [Fig. 5(a)] yields $K_1 = 0.25$ and $K_2 = 0.13$ erg/cm³ ($K_1 = 0.025$ and $K_2 = 0.013$ MJ/m³) at $T = 5$ K. K_1 is of the same order of magnitude as iron metal ($K_1 \simeq 0.48$ erg/cm³ [39]). Figure 6 shows

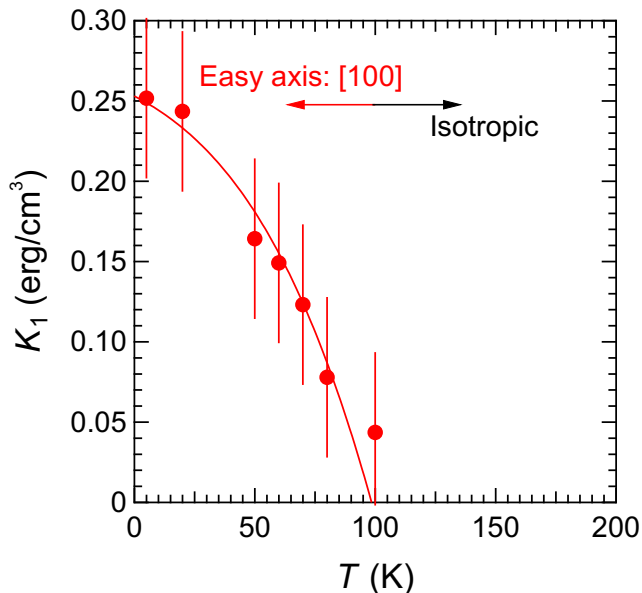


FIG. 6: Temperature dependence of the magnetocrystalline anisotropy constant K_1 of LuInCo_4 .

the temperature dependence of K_1 , which decreases monotonically with the increasing temperature and reaches 0 at $T \simeq 100$ K. This dependence demonstrates that the magnetic anisotropy changes from the easy magnetization axis along the [100] direction to isotropic as shown in Fig. 5.

2. Metamagnetic transition at low temperature

From inset of the Fig. 3 we can see a small increase in the magnetization at $H \simeq 1.4$ kOe only in the [111] direction. This anomaly can be clearly observed as a peak in its field derivative [Fig. 7]. The peak of dM/dH changes to a shoulder shape with raising temperature, and the metamagnetic-like bulge changes to a kink. The anomaly of dM/dH shifts to lower fields and disappears at $T \simeq 100$ K, where the magnetization becomes isotropic [Fig. 6]. This feature is different from that expected for a standard ferromagnet, suggesting the presence of different magnetic phases.

3. Critical scaling analysis of magnetization

To precisely determine the Curie temperature and to study the critical behavior of LuInCo_4 , a standard Arrott plot (M^2 vs. H/M) was performed using field-dependent magnetization data measured at $T = 275$ – 350 K [Fig. 8(a)]. The Arrott plots have positive slope, in accordance with the nature of the second order transition. Based

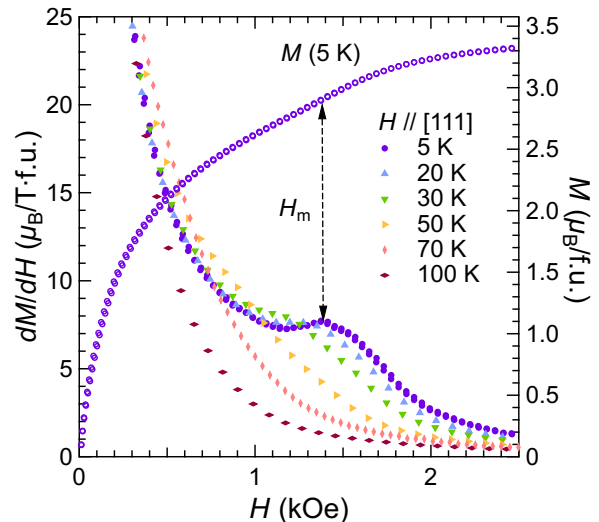


FIG. 7: Field derivative of the magnetization curve of LuInCo_4 with the field applied in the [111] direction. Open circles show the magnetization curve at $T = 5$ K.

on the mean-field approximation, the Arrott plot at T_C should be straight and pass through the origin. As can be seen in Fig. 8(a), it is not linear at low field, suggesting that the mean-field theory is too simple to explain the magnetism of LuInCo_4 . This deviation may be ascribed to the neglected electron correlations and spin fluctuations, which are significant in itinerant ferromagnets. To better describe the magnetization process, a generalized Arrott plot (GAP) is known to be effective. A generalized Arrott plot is derived from the Arrott-Noaks equation of state [40],

$$\left(\frac{H}{M}\right)^{\frac{1}{\gamma}} = a\epsilon + BM^{\frac{1}{\beta}}, \quad (4)$$

where β and γ are the critical exponents, and the reduced temperature ϵ is given by $\epsilon = (T - T_C)/T_C$. Using β and γ , the spontaneous magnetization M_s and the inverse initial susceptibility χ_0^{-1} are described by the power laws [41],

$$M_s(T) = M_0(-\epsilon)^\beta, \quad T < T_C \quad (\epsilon < 0), \quad (5)$$

$$\chi_0^{-1}(T) = \left(\frac{H}{M_0}\right)\epsilon^\beta, \quad T > T_C \quad (\epsilon > 0), \quad (6)$$

where M_0 and H/M_0 are the critical amplitudes. $M_s(T)$ and $\chi_0^{-1}(T)$ are estimated from the X- and Y-intercepts of the extrapolated lines in the high field region of the Arrott plots, respectively. First, we obtained $\beta = 0.54$ and $\gamma = 0.98$ from $M_s(T)$ and $\chi_0^{-1}(T)$ estimated from the standard Arrott plots using the Eqs. (5) and (6), and used them to construct the modified Arrott plots. Again, we estimated $M_s(T)$ and $\chi_0^{-1}(T)$ from the established modified Arrott plots to obtain the critical exponents. This procedure was iterated until straight lines at $T \simeq T_C$

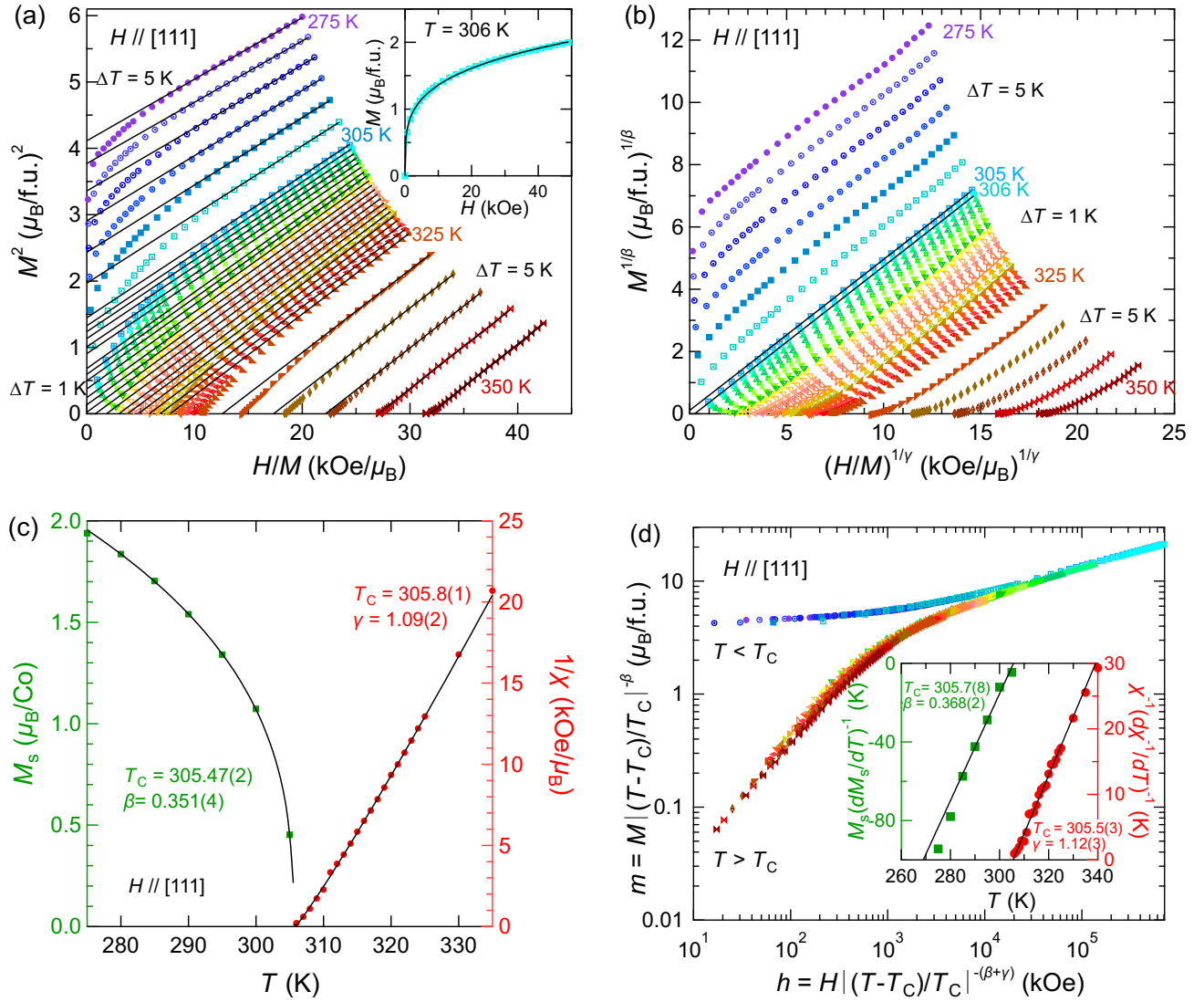


FIG. 8: (a) The standard Arrott plots. The inset shows the isothermal magnetization at $T = 306$ K and the fitting results of $M = H^\delta$ with $\delta = 4.08$. (b) The final version of the generalized Arrott plots. (c) The temperature dependence of the spontaneous magnetization and inverse susceptibility obtained from the generalized Arrott plot. The lines represent the fit to the power function. (d) Scaling plots with β and γ determined by the KF method on both logarithmic scales. The inset shows the KF plots.

were obtained throughout the field range with unchanged critical exponents. Figure 8(b) shows the final Arrott plots $M^{1/\beta}$ vs. $(H/M)^{1/\gamma}$. A good linearity can be seen near T_C , indicating that the critical exponents have been properly estimated ($\beta = 0.351(3)$, $T_C = 305.47(3)$ K and $\gamma = 1.09(2)$, $T_C = 305.8(1)$ K).

An alternative method for estimating the values of β , γ and T_C is the Kouvel–Fisher (KF) method [41]. Here, Eqs. (5) and (6) are reformulated as

$$M_s(T)[dM_s(T)/dT]^{-1} = (T - T_C)\beta^{-1}, \quad T < T_C \quad (\epsilon < 0), \quad (7)$$

$$\chi_0^{-1}(T)[d\chi_0^{-1}(T)/dT]^{-1} = (T - T_C)\gamma^{-1}, \quad T > T_C \quad (\epsilon > 0). \quad (8)$$

β and γ can be calculated from the slope of $1/\beta$ and $1/\gamma$, and T_C from the X-intercept in the plots of $M_s(T)[dM_s(T)/dT]^{-1}$ vs. T and $\chi_0^{-1}(T)[d\chi_0^{-1}(T)/dT]^{-1}$ vs. T , respectively [Fig. 8(c)]. Linear fits to Eqs. (7) and (8) yield $\beta = 0.37(2)$, $T_C = 305.7(8)$ K and $\gamma = 1.12(3)$, $T_C = 305.5(3)$ K, respectively, which are close to those estimated from power-function fits. The small variation in β is probably due to the limited magnetization data for $T < T_C$.

Finally, the critical exponent δ can be calculated using the equation [41]

$$M \propto H^{1/\delta}. \quad (9)$$

The fit yields $\delta = 4.08(3)$ [inset of Fig. 8(a)], which is close to that estimated by the Widom relation $\delta = 1 + \frac{\gamma}{\beta}$ [42] (4.11(6) from the generalized Arrott plot and 4.03(22) from the KF method). Based on the scaling hypothesis of the second order phase transition [43], the asymptotic equation of state near the transition temperature, the scaling form of the temperature-dependent magnetization is given by

$$m = f_{\pm}(h), \quad (10)$$

where

$$m = |\epsilon|^{-\beta} M(H, \epsilon) \quad \text{and} \quad h = H |\epsilon|^{-(\beta+\gamma)}. \quad (11)$$

$f_+(T < T_C)$ and $f_-(T > T_C)$ are the regular functions. Figure 8(d) shows the scaling plot m vs. h on both logarithmic scales obtained by using the critical exponents estimated by the KF method. The scaling curve is divided into two parts: the upper one is for $T < T_C$ and the lower one is for $T > T_C$, showing that the critical exponents β and γ and the Curie temperature T_C have been properly estimated.

The obtained critical exponents satisfy none of the known universality classes, such as mean-field ($\beta = 0.5$, $\gamma = 1$, $\delta = 3$), three-dimensional (3D) Ising ($\beta = 0.326$, $\gamma = 1.238$, $\delta = 4.80$), 3D XY ($\beta = 0.345$, $\gamma = 1.316$, $\delta = 4.81$), and 3D Heisenberg model ($\beta = 0.367$, $\gamma = 1.388$, $\delta = 4.78$). While β is close to the values in the three-dimensional universality class [44], γ is between the mean-field and three-dimensional universality classes. The discrepancy may be due to magnetic interactions beyond the nearest neighbor or short-range correlations.

4. Magnetocaloric properties

Because of the ferromagnetic ordering of LuInCo₄ near room temperature, it is worth evaluating its magnetocaloric properties. The isothermal entropy change due to the application of a magnetic field $\Delta S_M(T, M) = S(T, H) - S(T, 0)$ is calculated by integrating the Maxwell relation as

$$\Delta S_M = \int_0^H (\partial M / \partial T)_{H'} dH'. \quad (12)$$

In the real measurement of isothermal magnetization at a small step of field ΔH , with a small temperature interval $T_2 - T_1$, ΔS_M can be written by

$$\Delta S_M \left(\frac{T_1 + T_2}{2}, H \right) = \sum \left[\frac{M(T_2, H) - M(T_1, H)}{T_2 - T_1} \right] \Delta H. \quad (13)$$

Figure 9 shows the temperature dependence of ΔS_M estimated from the field-dependent magnetization data at different temperatures around T_C under the field

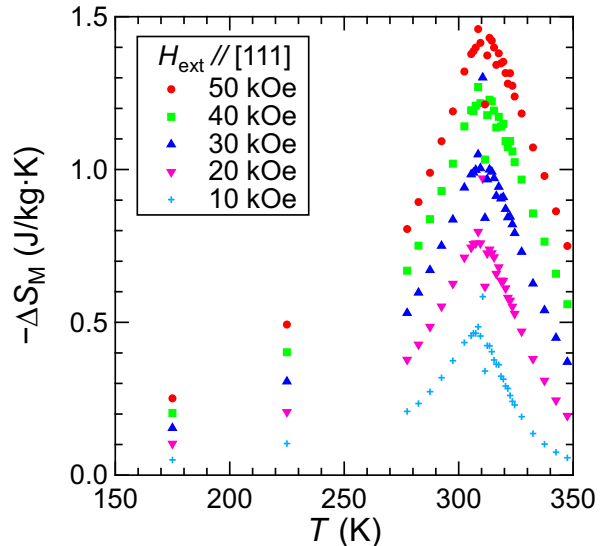


FIG. 9: Temperature dependence of the magnetic entropy change ΔS_M at selected fields applied in the [111] direction.

applied in the [111] direction. The maximum entropy change $-\Delta S_{M,\max}$ related to the ferromagnetic ordering is indeed observed around the Curie temperature $T \simeq 310$ K. The calculated values of $-\Delta S_{M,\max}$ are 0.80(5) and 1.45(5) J/kg·K for a field change of 0–2 T and 0–5 T, respectively. The maximum relative cooling power (RCP) is calculated as the product of the maximum entropy change $-\Delta S_{M,\max}$ and the full-width at half-maximum of the ΔS_M peak. The RCP values are estimated to be 30 and 105 J/kg, respectively.

IV. FIRST-PRINCIPLE CALCULATIONS

We have calculated the electronic structures in the spin-polarized (SP) and spin-unpolarized (NM) states to verify the ferromagnetic nature of LuInCo₄. A comparison of the estimated total energies predicts that the SP state is more stable with a total energy 0.34 eV/f.u. lower than that of the NM state. The calculated equilibrium lattice parameters for the NM and SP states are $a_{\text{NM}} = 6.9333$ Å and $a_{\text{SP}} = 6.9997$ Å, respectively. The latter is in better agreement with the experimental value (7.0387 Å) obtained from XRD measurements at room temperature. Figure 10 shows the total DOS and the site-composed DOS of the SP state. The DOS near the Fermi energy (E_F) and the large band splitting are mainly due to the Co-3d bands, which dominantly contribute to the ferromagnetic nature of LuInCo₄. Similarly, the Lu-5d DOS is found to split, which is caused by the hybridization between Co-3d and Lu-5d bands. The magnetic moment of each atom is

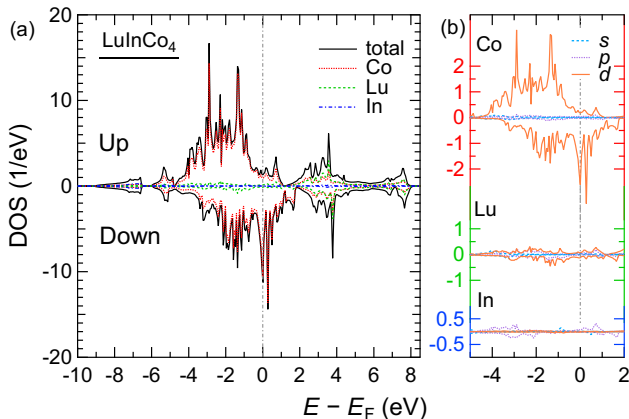


FIG. 10: (a) Total and (b) site-decomposed DOS at each atomic site in the spin-polarized state of LuInCo_4 obtained from DFT calculations.

calculated to be $\mu_{\text{Co}} = 1.290 \mu_{\text{B}}$, $\mu_{\text{Lu}} = -0.274$, and $\mu_{\text{In}} = -0.042$. The total magnetic moment of $4.843 \mu_{\text{B}}$ is slightly larger but comparable to the experimental value estimated by magnetization measurements ($3.43 \mu_{\text{B}}$). Although the value of μ_{Co} is not currently observed experimentally, it is close to the value obtained for YMgCo_4 by DFT calculations ($\mu_{\text{Co}} = 1.39 \mu_{\text{B}}$ [21]) and for LuFe_2 by neutron diffraction (ND) measurements ($\mu_{\text{Fe}} = 1.7 \mu_{\text{B}}$ [45, 46]). We find that the Lu atom has a non-negligible magnetic moment, antiparallel to the Co moment, induced by the spin polarization of the Lu-5d bands. It is well known that in such magnets containing 3d transition metal elements and 5d (4d) transition metal or rare earth elements, 3d-5d (4d) hybridization plays an important role in the antiferromagnetic coupling between them [47–49]. When the 3d bands are spin-polarized, the energy of the 3d-local DOS of the down spins becomes closer to the 5d-local DOS, which is at a higher energy level. Therefore, the 5d-3d hybridization becomes stronger for down spin electrons, leading to the larger number of 5d electrons with down spins below E_{F} . Although not yet detected for LuInCo_4 , the presence of the magnetic moment μ_{Lu} has been revealed by ^{175}Lu -NMR measurement in LuFe_2 [50], and the ferrimagnetic structure between the Lu and Fe sublattices has been observed by spin-polarized ND [45] and x-ray magnetic circular dichroism (XMCD) measurements [51, 52].

Figures 11(a) and 11(c) show the down-spin and up-spin band structures, respectively. The orbital-resolved Co-3d DOS is also shown in Fig. 11(b). In LuInCo_4 , the Co atoms form a pyrochlore lattice. As it contains three-dimensional stacking of the four equivalent $\{111\}$ -kagome planes, the pyrochlore lattice can host three-dimensional flat bands throughout the Brillouin zone generated by destructive quantum interference of electron hopping [9, 53, 54]. We found multiple narrow bands, as highlighted by the rectangular boxes

in Figs. 11(a) and 11(c). Just above the E_{F} for the down-spin channel, narrow bands lie along the K- Γ -L path, forming a sharp peak of the Co-3d DOS [Fig. 11(b)]. We can see from Fig. 11(b) that all d orbitals contribute to the narrow bands. The corresponding bands for the up-spin channel appear at ~ -1.3 eV, showing a splitting of ~ 1.3 eV by spin polarization. Interestingly, the bands are almost flat, suggesting localized states of the electrons reflecting the geometry of the pyrochlore lattice. Above these narrow bands, the DOS curve also has sharp peaks at ~ 0.25 and -1.1 eV for the down- and up-spin channels, respectively, which are attributed to narrow bands along the L-U and L-K paths. They are found to consist mainly of the $d_{x^2-y^2}$ orbital. Consequently, such highly degenerate electronic states lead to a strong Stoner instability, which induces the ferromagnetic correlations.

Since the heavy atom Lu is involved, we employed the spin-orbit coupling (SOC) in the calculations. We calculated the total energy for the collinear ferromagnetic structure with the spin oriented in the [100], [110] and [111] directions. It resulted in the lowest energy for the [111] easy axis case with the energy difference of 2.5×10^{-6} eV/f.u. and 2.3×10^{-5} eV/f.u. with the [100] and [110] cases, respectively. The lattice parameters and magnetic moments are the same as without SOC. Considering the energy tolerance of 10^{-7} eV/f.u., it should be noted that the small energy difference is not accurate enough to discuss the spin orientation from DFT calculations, which may be affected by the initial parameters of the calculations. However, the detected small anisotropy is comparable to the experimental observation. Figure 11(d) shows the band structure and partial DOS of the Co-3d electrons calculated with SOC for the [100] easy axis. We observe the significant gap induced by SOC at the multiple band crossings and at the high-symmetry Γ and L points. The DOS is similar to that without SOC, including the occupancies of the orbitals. Note that similar results have been obtained for the [111] and [110] easy axes.

V. DISCUSSION

Figure 12 shows the magnetic phase diagram when the field is applied in the [111] direction as determined from the magnetization measurements. The temperature axis is plotted on a logarithmic scale. Remarkably, anisotropic ferromagnetic phases $\text{FM}_{\text{aniso}1}$ and $\text{FM}_{\text{aniso}2}$ appear below the temperature of $T \approx 100$ K, in addition to the isotropic ferromagnetic phase (FM_{iso}) just below the Curie temperature T_{C} . The $\text{FM}_{\text{aniso}1}$ phase is surrounded by the horizontal axis ($H = 0$) and the metamagnetic-transition fields H_{m} (solid curve). The $\text{FM}_{\text{aniso}2}$ phase is above the $\text{FM}_{\text{aniso}1}$ phase, surrounded by the H_{m} curve and the fields where the magnetization is saturated, H_{sat} , estimated from the second

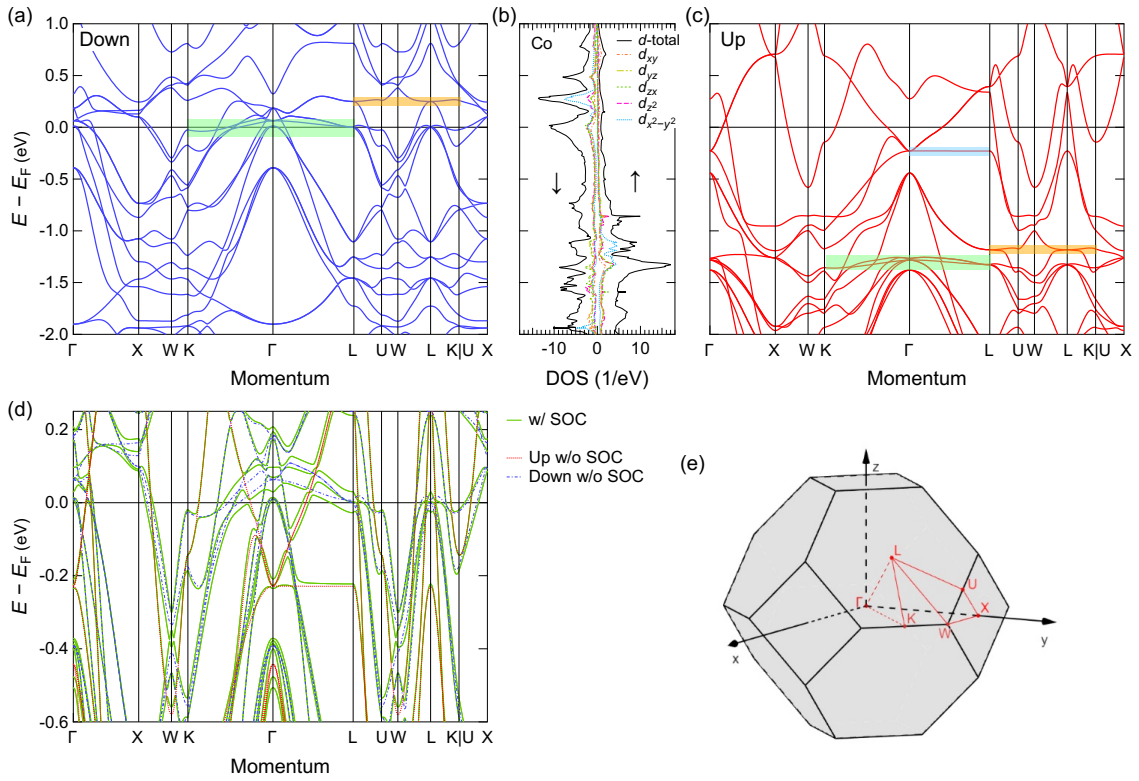


FIG. 11: Band structure with down-spin (a) and up-spin (c) channels without SOC. (b) Orbital-decomposed DOS at the Co site in the spin-polarized state of LuInCo₄. (d) Band structure with SOC when the [100] direction is the easy axis. (e) The first Brillouin zone of an FCC lattice.

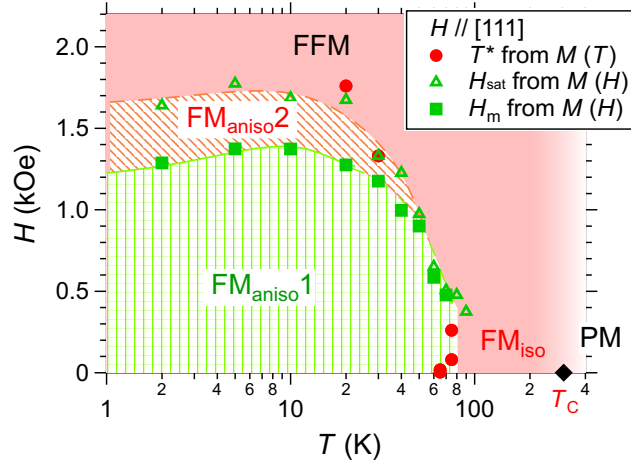


FIG. 12: Inferred magnetic phase diagram of LuInCo₄ under the field applied in the [111] direction. x -axis (temperature) is shown on a logarithmic scale.

field derivative d^2M/dH^2 (dashed curve). This curve corresponds approximately to the field-dependent T^* in the temperature derivative dM/dT [Fig. 4(b)]. Thus, the FM_{aniso2} phase is considered to be one in which the magnetization is not saturated as a feature of the hard

axis, and turns to the field-forced ferromagnetic (FFM) state. Above $T \simeq 100$ K, the magnetization is isotropic and quickly saturated, distinguishing the FM_{iso} phase from the FM_{aniso1} and FM_{aniso2} phases with the [111] hard axis.

Since the FM_{aniso1} phase has the large magnetization, three possible magnetic structures can be proposed. One is the collinear ferromagnetic structure, but with a smaller ordered moment than in the FFM phase. Due to the large 3d down-spin DOS peak near the E_F [Fig. 10], further instability and spin polarization can be induced by applying a magnetic field as a kind of itinerant metamagnetic transition [55, 56] only in the [111] direction, accompanied by a discontinuous increase of the ordered moment. Similar magnetization jumps are observed in the ferromagnets ThCo₅ [57], YCo₃ [58], and LuCo₃ [59]. This is reasonable because the down-spin bands lie along the $\Gamma(0,0,0)$ - $L(\frac{1}{2}, \frac{1}{2}, \frac{1}{2})$ direction [Fig. 11(a)]. Another is a weakly coupled ferrimagnetic structure between the Lu and Co sublattices. Although DFT calculations suggest that the ferrimagnetism is stable in the ground state, due to the weak magnetocrystalline anisotropy with $K_1 = 0.25$ erg/cm³, the Lu spins can be easily rotated toward the applied field direction and undergo a spin-flop transition when the field is applied in the [111] hard magnetization direction. From the magnetization

curve at $T = 5$ K, the increase in magnetization at the metamagnetic transition could be roughly calculated to be $\sim 0.2 \mu_B/\text{f.u.}$, which is of the same order of magnitude as μ_{Lu} predicted by DFT calculations. The other is the noncollinear structure of the Co sublattice, where the magnetic moments are practically ferromagnetic but have a small antiferromagnetic component. At the applied field of H_m , the spins rotate towards the collinear ferromagnetic configuration (FFM). Here, we assume the situation with the nearest neighbor ferromagnetic coupling and the uniaxial magnetocrystalline anisotropy along the $\langle 111 \rangle$ directions. This is because the Co site forming the pyrochlore lattice is crystallographically unique with the locally trigonal symmetry axis along $\langle 111 \rangle$. Therefore, when the anisotropy is dominant, the moment at each Co site is constrained along four different symmetry directions, $[\bar{1}11]$, $[1\bar{1}1]$, $[11\bar{1}]$, and $[111]$, that is the spin-ice state [60]. In this state, the $[100]$, $[110]$, and $[111]$ directions are known to become the easy, hard, and hardest magnetization directions, respectively, with the different saturation magnetization ($4/\sqrt{3}\mu_{\text{Co}}$, $2\sqrt{2/3}\mu_{\text{Co}}$, and $2\mu_{\text{Co}}/\text{f.u.}$, respectively), and the metamagnetic transition occurs along the $[111]$ direction [61, 62]. Except for the uniform saturation magnetization in all measured directions, the observed magnetization curves of LuInCo_4 at low temperature are similar to the feature of the spin-ice state. This suggests that the $\text{FM}_{\text{aniso1}}$ phase may have unconventional spin-ice correlations as in ice-like splayed ferromagnetism [63–65], possibly due to the itinerant nature of the Co-3d electrons and the insufficient uniaxial anisotropy. To gain a deeper insight, it is desirable to study the magnetization evolution at the lower temperature.

VI. CONCLUSION

We have successfully synthesized single crystals of the site-ordered cubic (C15b) Laves phase compound LuInCo_4 with a Co-pyrochlore sublattice. Magnetization measurements revealed that LuInCo_4 is a ferromagnet with $T_C = 306$ K and $M_{\text{sat}} = 3.43 \mu_B/\text{f.u.}$ at $T = 5$ K. DFT calculations predicted that the Co and Lu sublattices are antiferromagnetically coupled in the ground state, verifying the experimentally observed ferromagnetic nature. At high temperature the magnetization shows isotropic behavior, while at low temperature it exhibits magnetocrystalline anisotropy with the easy magnetization axis in the $[100]$ direction. Moreover, the magnetization shows unusual ferromagnetic behavior: a metamagnetic transition in the $[111]$ direction below the temperature where the magnetization becomes anisotropic, and critical behavior deviating from known universality classes.

The indicated magnetically ordered phases in the low- T and H region and the multiple flat bands near the Fermi level makes LuInCo_4 an interesting ferromagnet from the point of view of the new frustrated and topological pyrochlore metals. To reveal the microscopic magnetism at low temperature is highly desirable, for example by the neutron diffraction and nuclear magnetic resonance measurements on a single crystal.

ACKNOWLEDGMENTS

This work was supported by JSPS KAKENHI Grant No. JP24KJ1325.

-
- [1] A. P. Ramirez, A. Hayashi, R. J. Cava, R. Siddharthan, and B. S. Shastry, *Nature* **399**, 333 (1999).
- [2] M. J. Harris, S. T. Bramwell, D. F. McMorrow, T. Zeiske, and K. W. Godfrey, *Phys. Rev. Lett.* **79**, 2554 (1997).
- [3] M. J. P. Gingras, C. V. Stager, N. P. Raju, B. D. Gaulin, and J. E. Greedan, *Phys. Rev. Lett.* **78**, 947 (1997).
- [4] J. S. Gardner, S. R. Dunsiger, B. D. Gaulin, M. J. P. Gingras, J. E. Greedan, R. F. Kiefl, M. D. Lumsden, W. A. MacFarlane, N. P. Raju, J. E. Sonier, I. Swainson, and Z. Tun, *Phys. Rev. Lett.* **82**, 1012 (1999).
- [5] R. Ballou, J. Deportes, R. Lemaire, Y. Nakamura, and B. Ouladdiaf, *J. Magn. Magn. Mater.* **70**, 129 (1987).
- [6] M. Shiga, K. Fujisawa, and H. Wada, *J. Phys. Soc. Jpn.* **62**, 1329 (1993).
- [7] K. Essafi, L. D. C. Jaubert, and M. Udagawa, *J. Phys.: Condens. Matter* **29**, 315802 (2017).
- [8] I. Hase, T. Yanagisawa, Y. Aiura, and K. Kawashima, *Phys. Rev. Lett.* **120**, 196401 (2018).
- [9] J. P. Wakefield, M. Kang, P. M. Neves, D. Oh, S. Fang, R. McTigue, S. Y. Frank Zhao, T. N. Lamichhane, A. Chen, S. Lee, S. Park, J.-H. Park, C. Jozwiak, A. Bostwick, E. Rotenberg, A. Rajapitamahuni, E. Vescovo, J. L. McChesney, D. Graf, J. C. Palmstrom, T. Suzuki, M. Li, R. Comin, and J. G. Checkelsky, *Nature* **623**, 301 (2023).
- [10] J. Huang, L. Chen, Y. Huang, C. Setty, B. Gao, Y. Shi, Z. Liu, Y. Zhang, T. Yilmaz, E. Vescovo, M. Hashimoto, D. Lu, B. I. Yakobson, P. Dai, J.-H. Chu, Q. Si, and M. Yi, *Nat. Phys.* **20**, 603 (2024).
- [11] L. Fu, C. L. Kane, and E. J. Mele, *Phys. Rev. Lett.* **98**, 106803 (2007).
- [12] S. M. Young, S. Zaheer, J. C. Y. Teo, C. L. Kane, E. J. Mele, and A. M. Rappe, *Phys. Rev. Lett.* **108**, 140405 (2012).
- [13] X. Wan, A. M. Turner, A. Vishwanath, and S. Y. Savrasov, *Phys. Rev. B* **83**, 205101 (2011).
- [14] E. Gratz and A. S. Markosyan, *J. Phys.: Condens. Matter* **13**, R385 (2001).
- [15] T. Goto, K. Fukamichi, T. Sakakibara, and H. Komatsu, *Solid State Commun.* **72**, 945 (1989).

- [16] T. Goto, T. Sakakibara, K. Murata, H. Komatsu, and K. Fukamichi, *J. Magn. Magn. Mater.* **90-91**, 700 (1990).
- [17] R. Lemaire, *Cobalt* **33**, 201 (1986).
- [18] E. Burzo and J. Laforest, *Int. J. Magn.* **3**, 171 (1972).
- [19] Q.-Q. Jin and S.-B. Mi, *J. Alloys Compd.* **582**, 130 (2014).
- [20] V. Shtender, R. Denys, V. Paul-Boncour, A. Riabov, and I. Zavaliy, *J. Alloys Compd.* **603**, 7 (2014).
- [21] T. Shiotani, H. Ohta, T. Waki, Y. Hashimoto, Y. Tabata, and H. Nakamura, *J. Alloys Compd.* **961**, 170990 (2023).
- [22] R. Denys, A. Riabov, R. Černý, I. Koval'chuk, and I. Zavaliy, *J. Solid State Chem.* **187**, 1 (2012).
- [23] V. Paul-Boncour, P. Beran, C. Hervoches, and V. Shtender, *ACS Omega* **8**, 30727 (2023).
- [24] M. K. Reimann, M. Johnscher, T. Block, J. Bönninghausen, and R. Pöttgen, *Z. Naturforsch. B* **78**, 497 (2023).
- [25] L. V. Sysa, V. I. Zaremba, Y. M. Kalychak, and Y. M. Baranyak, *Visnyk Lviv University, Ser. Khim* **29**, 32 (1988).
- [26] F. Izumi and K. Momma, *Solid State Phenom.* **130**, 15 (2007).
- [27] G. Kresse and J. Hafner, *Phys. Rev. B* **47**, 558 (1993).
- [28] G. Kresse and J. Hafner, *Phys. Rev. B* **49**, 14251 (1994).
- [29] G. Kresse and J. Furthmüller, *Comput. Mat. Sci.* **6**, 15 (1996).
- [30] G. Kresse and J. Furthmüller, *Phys. Rev. B* **54**, 11169 (1996).
- [31] P. E. Blöchl, *Phys. Rev. B* **50**, 17953 (1994).
- [32] G. Kresse and D. Joubert, *Phys. Rev. B* **59**, 1758 (1999).
- [33] J. P. Perdew, K. Burke, and M. Ernzerhof, *Phys. Rev. Lett.* **77**, 3865 (1996).
- [34] W. H. Press, S. A. Teukolsky, W. T. Vetterling, and B. P. Flannery, *Numerical Recipes 3rd Edition: The Art of Scientific Computing*, 3rd ed. (Cambridge University Press, 2007).
- [35] P. E. Blöchl, O. Jepsen, and O. K. Andersen, *Phys. Rev. B* **49**, 16223 (1994).
- [36] M. Methfessel and A. T. Paxton, *Phys. Rev. B* **40**, 3616 (1989).
- [37] C. Moriyoshi, S. Shimomura, K. Itoh, K. Kojima, and K. Hiraoka, *J. Magn. Magn. Mater.* **260**, 206 (2003).
- [38] K. Murata, K. Fukamichi, Y. Fujinaga, Y. Syono, and T. Goto, *J. Magn. Magn. Mater.* **140-144**, 833 (1995).
- [39] S. Blundell, *Magnetism in Condensed Matter* (Oxford University Press, Oxford, 2001).
- [40] A. Arrott and J. E. Noakes, *Phys. Rev. Lett.* **19**, 786 (1967).
- [41] J. S. Kouvel and M. E. Fisher, *Phys. Rev.* **136**, A1626 (1964).
- [42] B. Widom, *J. Chem. Phys.* **43**, 3898 (1965).
- [43] H. E. Stanley, *Introduction to Phase Transitions and Critical Phenomena* (Oxford University Press, New York, 1971).
- [44] M. F. Collins, *Magnetic critical scattering* (Oxford University Press, Oxford, 1989).
- [45] A. Murani, *Physica B* **345**, 89 (2004).
- [46] D. Givord, A. Gregory, and J. Schweizer, *J. Magn. Magn. Mater.* **15-18**, 293 (1980).
- [47] H. Yamada, *Physica B+C* **149**, 390 (1988).
- [48] M. S. S. Brooks, O. Eriksson, and B. Johansson, *J. Phys.: Condens. Matter* **1**, 5861 (1989).
- [49] M. S. S. Brooks, L. Nordstrom, and B. Johansson, *J. Phys.: Condens. Matter* **3**, 2357 (1991).
- [50] Y. Kasamatsu, J. Armitage, J. Lord, P. Riedi, and D. Fort, *J. Magn. Magn. Mater.* **140-144**, 819 (1995).
- [51] C. Giorgetti, S. Pizzini, E. Dartyge, A. Fontaine, F. Baudet, C. Brouder, P. Bauer, G. Krill, S. Miraglia, D. Fruchart, and J. P. Kappler, *Phys. Rev. B* **48**, 12732 (1993).
- [52] M. A. Laguna-Marco, J. Chaboy, and C. Piquer, *Phys. Rev. B* **77**, 125132 (2008).
- [53] H.-M. Guo and M. Franz, *Phys. Rev. Lett.* **103**, 206805 (2009).
- [54] D. L. Bergman, C. Wu, and L. Balents, *Phys. Rev. B* **78**, 125104 (2008).
- [55] Shimizu, M., *J. Phys. France* **43**, 155 (1982).
- [56] H. Yamada, K. Fukamichi, and T. Goto, *Physica B* **327**, 148 (2003).
- [57] D. Givord, J. Laforest, and R. Lemaire, *J. Appl. Phys.* **50**, 7489 (1979).
- [58] T. Goto, H. Katori, T. Sakakibara, and M. Yamaguchi, *Physica B* **177**, 255 (1992).
- [59] D. S. Neznakhin, D. I. Radzivonchik, D. I. Gorbunov, A. V. Andreev, J. Šebek, A. V. Lukoyanov, and M. I. Bartashevich, *Phys. Rev. B* **101**, 224432 (2020).
- [60] S. T. Bramwell and M. J. P. Gingras, *Science* **294**, 1495 (2001).
- [61] R. Moessner and S. L. Sondhi, *Phys. Rev. B* **68**, 064411 (2003).
- [62] S. V. Isakov, K. S. Raman, R. Moessner, and S. L. Sondhi, *Phys. Rev. B* **70**, 104418 (2004).
- [63] J. Gaudet, K. A. Ross, E. Kermarrec, N. P. Butch, G. Ehlers, H. A. Dabkowska, and B. D. Gaulin, *Phys. Rev. B* **93**, 064406 (2016).
- [64] A. Yaouanc, P. Dalmas de Réotier, P. Bonville, J. A. Hodges, V. Glazkov, L. Keller, V. Sikolenko, M. Bartkowiak, A. Amato, C. Baines, P. J. C. King, P. C. M. Gubbens, and A. Forget, *Phys. Rev. Lett.* **110**, 127207 (2013).
- [65] S. Säubert, A. Scheie, C. Duvina, J. Kindervater, S. Zhang, H. J. Changlani, G. Xu, S. M. Koohpayeh, O. Tchernyshyov, C. L. Broholm, and C. Pfleiderer, *Phys. Rev. B* **101**, 174434 (2020).